Lattice numerical study of $q\bar{q}$ system near to the deconfinement phase transition

Sodbileg Chagdaa[1,*], Enkhtuya Galsandorj[1], Edwin Laermann[2] and Battogtokh Purev[1]

[1]*Department of Theoretical Physics, Institute of Physics and Technology, Mongolian Academy of Sciences, Peace Ave. 54b, 13330 Ulaanbaatar, Mongolia*

[2]*Fakultät für Physik, Universität Bielefeld, D-33615 Bielefeld, Germany*

We study the profiles of the flux tube between a static quark and an antiquark in quenched SU(2) lattice gauge theory at temperatures around the deconfinement phase transition. The physical width of the flux tube and the string tension have been determined from the transverse profiles and the $q\bar{q}$ potential, respectively. Exploiting the computational power of a GPU accelerator in our flux tube investigation, we achieve a much higher statistics through which we can increase the signal to noise ratio of our observables in the simulation. This has allowed to investigate larger lattices as well as larger separations between the quarks than in our previous work. The improved accuracy gives us better results for the width and the string tension. The physical width of the flux tube is increasing with the temperature up to around T_c while keeping its increasing dependence on the $q\bar{q}$ separation. The string tension results have been compared for two different sizes of the lattice. As the lattice becomes larger and finer together with the precision improved, the temperature dependent string tension tends to have smaller value than the previous one.

PACS numbers: 11.15.Ha, 12.38.Gc

I. INTRODUCTION

The study of properties of matter at high temperatures is a challenging topic in experimental as well as theoretical high energy physics since these are relevant for heavy ion collision experiments and for cosmology. The fundamental theory of matter which governs the physics at such extreme conditions is Quantum Chromodynamics (QCD), the theory of strongly interacting quarks and gluons. While quarks carry a color charge, all physically observed states so far are color singlets. All attempts to separate a quark from hadrons i.e. from bound quark states have failed. This is called quark confinement whose mechanism still has not yet been explained completely.

Quarks are sources of chromoelectric flux. It is generally believed that due to the non-abelian nature of the gauge interactions in QCD the flux between quarks inside a meson is squeezed into narrow tubes connecting the quarks. For an infinitely narrow flux, a string, confinement would manifest itself in an attractive, linearly rising potential between a static quark and antiquark pair. Thus the detailed investigation of the flux tube can give us more information on the confinement problem.

Already quite early, Hagedorn conjectured the break-down of ordinary hadron physics at some temperature. Due to asymptotic freedom of QCD [1, 2] it was also predicted that QCD at infinite temperature is a theory of asymptotically free and thus deconfined quarks and gluons. Indeed, most of the first numerical simulations of lattice regularized QCD at finite temperature indicated a transition from confined to deconfined quarks [3, 4], at a temperature which fairly recently has been determined as about 154 MeV [5, 6] in lattice simulations at the physical quark masses. The analysis of the flux tube between static quarks at high temperature, its energy per unit length and its width, is thus an interesting exploration ground to investigate confinement and the loss thereof.

The pure glue approximation of QCD, i.e. a SU(3) Yang-Mills theory, has been shown to develop a first order confinement-deconfinement transition at a critical temperature T_c. Correspondingly, the order parameter of this transition drops to 0 at T_c. In an SU(2) Yang-Mills theory, however, the transition is continuous. In full QCD, with dynamical quarks, the transition is a mere crossover at physical quark masses. Yet, it could be in the scaling region of a second order phase transition in the chiral limit. In any case, it is clear that also above T_c quarks and gluons will exhibit strong interactions. Thus, even at temperatures above T_c it is interesting to study the changes of the flux tube with temperature to obtain

* Electronic address: sodbileg@ipt.ac.mn

hints about QCD forces in this experimentally very important regime.

We study how the flux tube behaves when QCD undergoes the deconfining phase transition. To do so, we measure chromoelectric and chromomagnetic components of the field strength, stored in the flux tube, from Polyakov loop - plaquette correlations at various temperatures. From longitudinal and transverse profiles of the distribution of those components one can quantitatively analyze the temperature dependence of the physical width of the flux tube. The color averaged potential between a heavy quark and an antiquark at finite temperature allows us to determine the temperature dependent string tension values.

Such non-perturbative phenomena as quark confinement have successfully been studied using numerical simulations of lattice QCD. Formation and structure of the flux tube in SU(2) pure gauge theory have clearly been observed on the lattices and its chromo field distributions have extensively been investigated as a function of interquark distance and lattice volumes [7-10]. Based on the superconductivity picture, they confirm that in the confining phase the width of the flux tube is a physical quantity which is independent of the interquark distance. According to another conjecture [11-14], which is the string picture of confinement, it is assumed that in the confining phase the mean squared width of the flux tube should grow logarithmically as a function of interquark distance. Moreover, at finite temperature, close to the critical temperature, but still in the confining regime, it has been predicted in [15, 16] that the widening of the flux tube becomes linearly, not logarithmically dependent on the interquark distance. These authors have also show that the slope of the curve of this linear growth is an increasing function of the temperature. A recent calculation also by [17] showed that the intrinsic width of the flux tube diverges as the deconfinement transition is approached. In our previous work [18] we have concluded that the mean squared width of the energy density, D_ε^2, gradually decreases with increasing temperature. Further we were concluding that the decrease of width and height of the transverse profiles at the same time shows gradual disappearance of the flux tube at and above T_c. A recent lattice Monte Carlo simulation of SU(3) pure gauge theory by [19] finds that as the temperature is increased towards and above the deconfinement temperature, the field strength value inside the flux tube gets smaller, while the shape of it does not vary appreciably across deconfinement. [19] presented also some evidence about the existence of flux-tube structures in the magnetic sector of the theory in the deconfined phase. A more recent study by [20] claims evidence for the non-existence of flux tubes at temperatures above the deconfinement temperature. Therefore, in summary, one needs to check these things together with the temperature dependent string tension carefully to ascertain the flux tube fate below as well as above the critical temperature.

Thus, in this paper, we extend and improve our previous results [18] by moving to larger lattices as well as by increasing our statistics considerably. In order to study the geometry of the color flux tube closer to the continuum physics, we also increase both in resolution of the underlying lattice and in the linear extent of the string, which means working with very large lattices.

Increasing the statistics is of great significance. The euclidean expectation values of Wilson loops and their products are the most natural quantities in non-abelian gauge theories that encode much of the physical information about the strength of the force between static color sources. However, expectation values of large Wilson loops and loop correlation functions are difficult to compute through numerical simulation, because the signal-to-noise ratio is very rapidly decreasing with growing loop sizes. These observables, can, however, only be extracted reliably if one is able to calculate the relevant expectation values accurately over a significant range of loop sizes and distances. Thus, one has to increase the statistics or use better computational strategies [21].

Here we speed-up the generation of the gauge field configurations by executing the simulation program on a GPU accelerator. The acceleration of the simulation enabled us to reach twice as larger separation with higher accuracy than we had before and it gives us better results on the width and string tension values of the confining flux tube through much larger statistics.

The paper is organized as follows. In Section 2, we give the lattice definition of the observables to be measured, the visualization of the flux tube geometry and the details of the simulation program with the parameter values at which the simulations have been performed are summarized. We present our results in Section 3, which has the four

subsections. In the first subsection we displayed the results from the lattice with $N_\tau = 6$. Here the longitudinal and transverse profiles of the chromoelectric component of the field strength in the flux tube have been plotted at some given values of $R\sqrt{\sigma}$ and T_c. Transverse size effect has also been checked here for the lattices of sizes $32 \times 12^2 \times 6$ and $32 \times 18^2 \times 6$. Then we shifted to a larger and finer lattice with $N_\tau = 8$ in the second subsection and the same observables have been plotted from this lattice at some given values of $R\sqrt{T}$ and T_c. In the third subsection, we calculate the half width squared of the flux tube as functions of interquark distance and temperature from both lattices with $N_\tau = 6$ and $N_\tau = 8$ and compare them with our previous results and with some recent results by other people. In the final subsection, the temperature dependent string tensions have been computed and compared with the leading behavior. Finally we conclude in Section 4.

II. LATTICE SET-UP

Chromoelectric and chromomagnetic components of the field strength in the flux tube can be extracted from Polyakov loop-plaquette correlations [22, 23]

$$f_{\mu\nu}(R,\vec{x}) = \frac{\beta}{a^4}\left[\frac{\langle L(0)L^+(R)\,\hat{\jmath}_{\mu\nu}(\vec{x})\rangle}{\langle L(0)L^+(R)\rangle} - \langle \hat{\jmath}_{\mu\nu}\rangle\right] \qquad (1)$$

where a is the lattice spacing and β is the coupling constant.

The time propagation of the two static quarks sitting at the distance R from each other is represented by the Polyakov loop $L(0)$ and its conjugate $L^+(R)$ at distance R, where

$$L(\vec{n}) \equiv \frac{1}{N_c}\mathrm{Tr}\prod_{\tau=1}^{N_\tau} U_4(\vec{n},\tau) \qquad (2)$$

is the mathematical expression of the Polyakov loop located at some spatial site $\vec{n}$. The plaquette variable $\hat{\jmath}_{\mu\nu}$ at distance $\boldsymbol{x}$ from the line connecting the $q\bar{q}$ pair, with the orientation μ,ν

$$\hat{\jmath}_{\mu\nu} = \frac{1}{N_C}\mathrm{Tr}\big(U_{\mu,\nu}\big) \qquad (3)$$

measures the field strength $f_{\mu\nu}$ in the flux tube when correlated to the Polyakov loop pair. Here $U_{\mu,\nu}$ is the product of four link variables around the boundary of the plaquette and N_c is the number of colors.

In the following we have chosen our coordinate system such that the quark and the antiquark are separated along the "1" direction. The subscript $||$ denotes the component that is oriented parallel to the axis connecting the two sources, while $\perp$ denotes the two components that are perpendicular to this axis. A sketch of the chosen flux tube geometry and the orientations of the six chromoelectric and chromomagnetic components is shown in Figure 1.

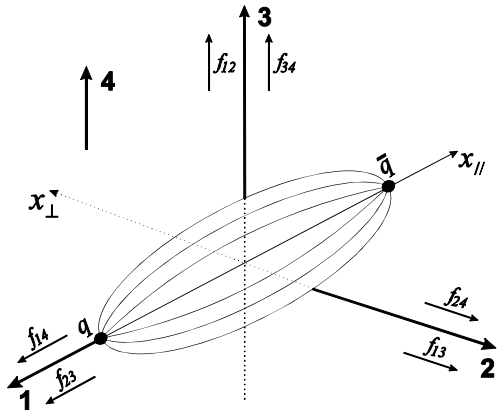

Figure 1. Sketch of the flux tube geometry.

The six different combinations of μ and ν define the six chromoelectric and chromomagnetic components of the field strength [24]. Three space-space plaquettes correspond to the magnetic components

$$f_{12} \to \frac{1}{2}(-B_\perp^2),\quad f_{13} \to \frac{1}{2}(-B_\perp^2),\quad f_{23} \to \frac{1}{2}\big(-B_{||}^2\big) \qquad (4)$$

and three space-time plaquettes correspond to the electric components

$$f_{24} \to \frac{1}{2}(E_\perp^2),\quad f_{34} \to \frac{1}{2}(E_\perp^2),\quad f_{14} \to \frac{1}{2}\big(E_{||}^2\big). \qquad (5)$$

One can then scan the profile of the flux tube by varying the position $\boldsymbol{x}$ of the plaquette. Our simulation program measures these six chromoelectric and chromomagnetic components by computing the correlations given by Equation 1. In our program, pure gauge theory with gauge group SU(2) with the standard Wilson action has been simulated on lattices of size $N_{||} \times N_\perp^2 \times N_\tau$ namely $32 \times 12^2 \times 6, 32 \times 18^2 \times 6,$ and $40 \times 16^2 \times 8$. Here $N_{||} > N_\perp$ due to our interest to have as large as possible $q\bar{q}$ separations along the $N_{||}$ direction.

The update algorithm is one heatbath [25-27] and four overrelaxation steps [28, 29]. For noise reduction we use the link integration method [30] and the reference point technique [31]. We have implemented the updates on a single Nvidia GPU accelerator, following the CUDA programming model for quenched SU(2) gauge theory of [32]. We have further implemented CUDA codes for the Polyakov loop-plaquette correlation that measures the flux tube [33].

The lattice regularization has a temporary role only. At the end, one has to convert the lattice results to physical units using the so-called scaling relation. For the determination of our scaling function we used the scaling relation based on the SU(2) zero temperature string tension results given by [34]. We prefer to give dimensionful quantities in units of σ, for the reason that the value of the SU(2) string tension in MeV is unknown.

The $q\bar{q}$ separation range at which the simulations have been performed is $0.3 - 2.3$ fm for the lattice of size $32 \times 12^2 \times 6$, $0.3 - 1.6$ fm for the lattice of size $32 \times 18^2 \times 6$ and $0.2 - 1.4$ fm for the lattice of size $40 \times 16^2 \times 8$. Exploiting the computational power of a GPU accelerator, we were able to increase the number of our measurements to 400000 for the first two lattices and 100000 for the third one. 10000 measurements have been used for the thermalization of the gauge configurations. Our simulation parameters and their values are summarized in Table 1.

Table 1. The values of the simulation parameters.

$N_{\|\|} \times N_\perp^2 \times N_\tau$	β	β_c	T/T_c	R/a	a[fm]	N_{me}
$32 \times 12^2 \times 6$	2.35	2.434	0.75	4 – 16	0.143	400 000
	2.39		0.86		0.125	
	2.43		0.98		0.109	
	2.47		1.13		0.095	
	2.51		1.29		0.083	
$32 \times 18^2 \times 6$	2.35	2.434	0.75	4 – 16	0.143	400 000
	2.39		0.86		0.125	
	2.43		0.98		0.109	
	2.47		1.13		0.095	
	2.51		1.29		0.083	
$40 \times 16^2 \times 8$	2.435	2.520	0.75	4 – 13	0.107	100 000
	2.475		0.86		0.093	
	2.515		0.98		0.082	
	2.560		1.13		0.070	
	2.600		1.29		0.062	

III. RESULTS

A. Flux tube profiles from the lattice with $N_\tau = 6$

Longitudinal profiles at $x_\perp = 0$ of the parallel electric component $1/2E_{||}^2(R,x)$ are displayed on the left column of Figure 2 at the given values of separation R. Their corresponding transverse profiles at $x_{||} = R/2$ are displayed on the right column of the figure at the same values of separation. The results have been plotted in units of the string tension.

Here we confirm with higher accuracy that at any $q\bar{q}$ separation $E_\perp \approx B_\perp \approx B_{||} < E_{||}$ [23] also at high temperature. Thus the force that tries to bind the q and $\bar{q}$ together is larger than the other forces in other directions. This holds for both longitudinal and transverse profiles. Since we have seen that the general T and R dependence is the same for all components, for convenience we have chosen to show only the parallel electric component, which is the largest one, in the following figures.

On the plots of the longitudinal profiles in Figure 2, one quark source is placed at $x_{||}\sqrt{\sigma} = 0$ and another one is at distance $R\sqrt{\sigma}$ from it. A longitudinal profile shows the general behavior that the field strength value has the peaks at the locations of q and $\bar{q}$ and decreases as the point at which the field strength is computed goes away from the sources. From Figure 2 one can also see that the field strength value at the middle point between the two sources decreases with rising temperature and the distribution approaches the one of two isolated quarks as the temperature goes to T_c. This is in agreement with the expectation that the flux tube exists only in the region below T_c. Increasing the separation accelerates this flux tube disappearing process with temperature.

Before we move to a smaller lattice spacing, we wanted to check that if there is an effect from transverse size of the lattice. To do so we have repeated our simulation on the lattice of size $32 \times 18^2 \times 6$ increasing only the transverse size of the lattice. Comparison of the results obtained from the two lattices differing with $N_\perp$ is shown in Figure 3 for various β at $R = 6a$. One can say from Figure 3 that for the given β and R, there are real differences between the values obtained at $N_\perp = 12$ and 18 because our data has significantly small error bars which do not overlap. The field strength value at larger $N_\perp$ is going to be greater than that at smaller $N_\perp$. The difference seems to grow when β decreases as it is clearly visible from the data at $\beta =$ 2.39 and 2.35. The transverse size effect becomes negligible when β approaches its critical value, $\beta_c =$ 2.43 in this figure.

B. Flux tube profiles from the lattice with $N_\tau = 8$

In the previous subsection we presented the results from $32 \times 12^2 \times 6$ lattice. After checking the transverse size effect we have chosen the next lattice size to be $40 \times 16^2 \times 8$. We have seen that the transverse size effect seems to appear to be strong in the confining phase well far from the critical coupling.

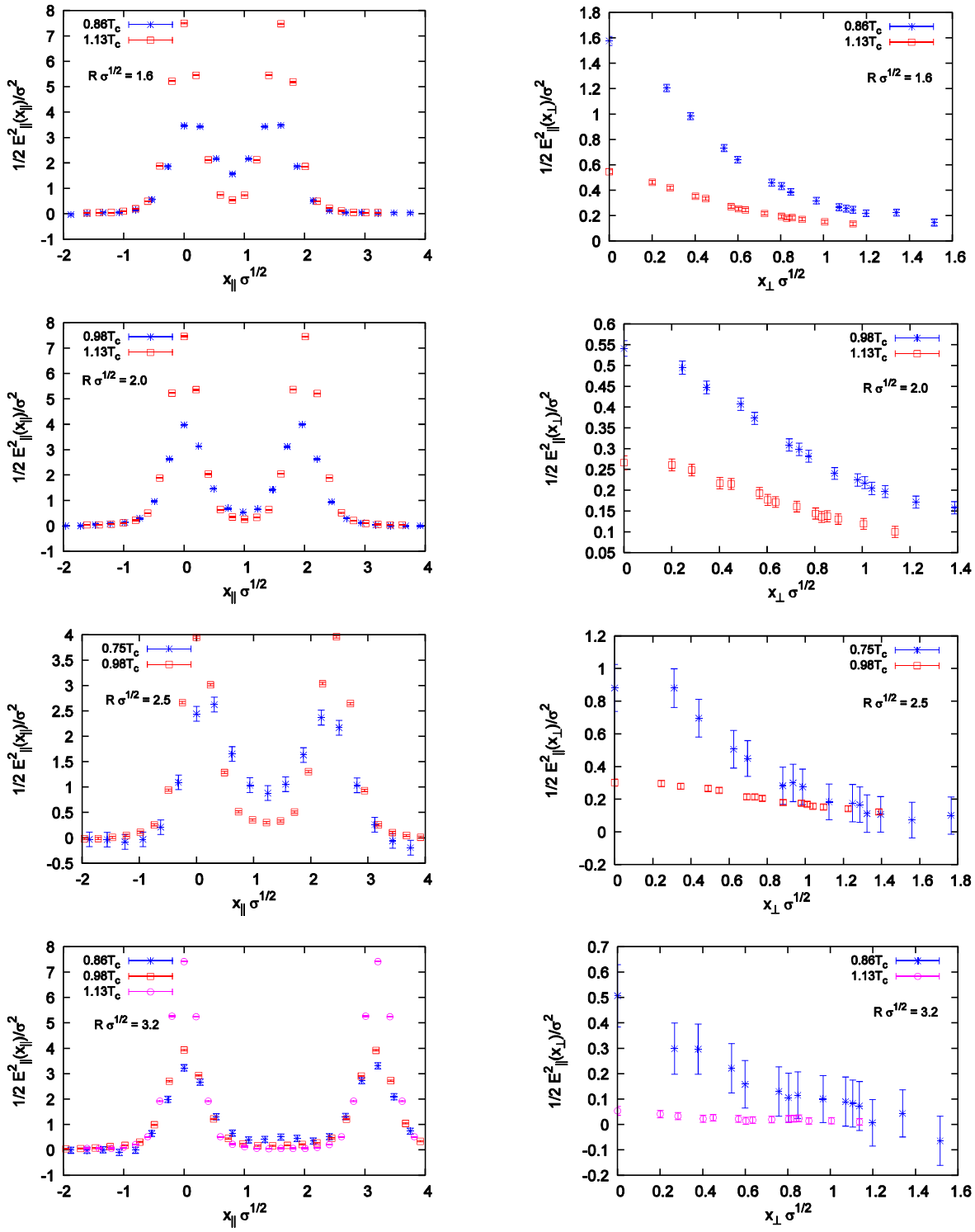

Figure 2. Left: Longitudinal profiles $1/2E_{||}^2(x_{||}, x_\perp = 0)$ *. Right: their transverse profiles* $1/2E_{||}^2(x_{||} = \frac{R}{2}, x_\perp)$ *at* $R\sqrt{\sigma} =$ $1.6, 2.0, 2.5$ *and* 3.2 *from the lattice of size* $32 \times 12^2 \times 6$.

And our region of interest is the close vicinity to the critical coupling where the effect is small but not negligible. Regarding all of this we changed $N_\perp$ from 12 to 16. Longitudinal and transverse profiles of the parallel chromoelectric component of the field strength in the flux tube obtained from the lattice of size $40 \times 16^2 \times 8$ at a given values of $R\sqrt{\sigma}$ and $T/T_c$are displayed in Figure 4.

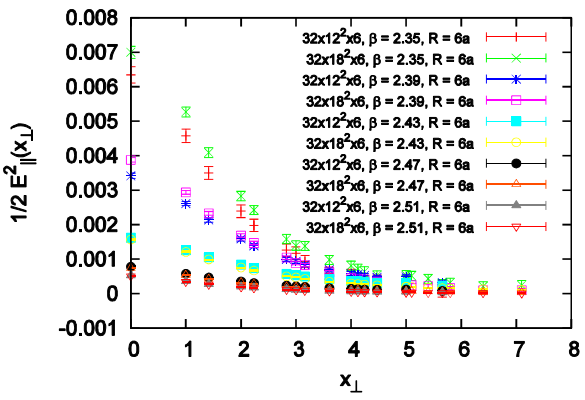

Figure 3. Checking transverse size effect by comparing the results obtained from two lattices differing only with $N_\perp$.

Note that the same color is used to denote the data that have been obtained at the same temperature value in all plots of Figure 4. The reason that, for a given value of $R\sqrt{\sigma}$ (in other words, from left to right direction), there are fewer data curves in a transverse plot than in a longitudinal one is that because we have to collect only those transverse profile data obtained at an even number of R/a, so that the transverse profiles can be at the middle plane between q and $\bar{q}$.

To summarize this chapter, in this work we were able to reach twice as larger separations with $4-5$ times smaller error bars than in our previous work. While the new results show the same temperature and distance dependence of the field strength or height of the flux tube like was in [18], the higher accuracy results from larger lattices redetermine the numerical value of the field strength. This leads us to redo the fits to determine the width and string tension of the flux tube.

C. Width of the flux tube

We call the width of the energy density the physical width of the flux tube. In principle, the width will be different at each $x_{||}$ point along the axis connecting q and $\bar{q}$. However, we prefer to choose the one at the middle transverse plane at $x_{||} = R/2$. The data on the middle transverse plane allow for fits to estimate the half width squared of the flux tube.

The half width squared, D_ε^2, can be quantitatively determined from the transverse profiles displayed in the right columns of Figure 2 and Figure 4 by fitting the data curves to appropriate fit functions. For small separation of the sources, perturbation theory is likely to apply and one might thus expect the distributions to follow the shape of the dipole field

$$f_{coul}(x_\perp) = \frac{a_1^{(\varepsilon)}}{(a_2^{(\varepsilon)} + x_\perp^2)^3} \tag{6}$$

and as the source separation becomes large, compared to the transverse size of the flux tube, the string picture comes into play and one might expect gaussian distributions like

$$f_{gaus}(x_\perp) = a_1^{(\varepsilon)} \exp\left(-a_2^{(\varepsilon)} x_\perp^2\right) \tag{7}$$

The upper index ε denotes fitting to energy density. The energy density $E^2 + B^2$ is given by $E_{||}^2 - B_{||}^2$ since we have seen from [23] that $\frac{1}{2}E_\perp^2(R, x_\perp) \approx -\frac{1}{2}B_\perp^2(R, x_\perp) \approx -\frac{1}{2}B_{||}^2(R, x_\perp)$ at the given values of β and R. We calculate the width of the energy density for each β and R. So we fit the average of the three approximately equal components, namely $-\frac{1}{2}B_{||}^2(R, x_\perp)$ and $\frac{1}{2}E_{||}^2(R, x_\perp)$ for each β and R. It turned out that the distribution of $-\frac{1}{2}B_{||}^2(R, x_\perp)$ is closely described by the coulombic fit function. And since we fit $E_{||}^2 - B_{||}^2$ for two regions of small and large separations, the functional form for $E_{||}^2 - B_{||}^2$ could be coulombic [8, 35]

$$-\frac{1}{2\beta}B_{||}^2(R, x_\perp) = \frac{a_1}{(a_2 + x_\perp^2)^3},$$
$$\frac{1}{2}E_{||}^2(R, x_\perp) = \frac{a_1}{(a_2 + x_\perp^2)^3} + \frac{a_1^{(\varepsilon)}}{\left(a_2^{(\varepsilon)} + x_\perp^2\right)^3} \tag{8}$$

for small separation $R_{phys} < 0.75$ fm and gaussian [8]

$$-\frac{1}{2\beta}B_{||}^2(R, x_\perp) = \frac{a_1}{(a_2 + x_\perp^2)^3},$$
$$\frac{1}{2}E_{||}^2(R, x_\perp) = \frac{a_1}{(a_2 + x_\perp^2)^3} + a_1^{(\varepsilon)} e^{-a_2^{(\varepsilon)} x_\perp^2} \tag{9}$$

for large separations $R_{phys} > 0.75$ fm.

The physical width of the flux tube is defined as [12, 35]

$$a^{-2}D_\varepsilon^2 = \frac{\int d^2x_\perp x_\perp^2 (E^2 + B^2)}{\int d^2x_\perp (E^2 + B^2)} \tag{10}$$

in terms of the fit parameters. After calculating the integrals it is given by

$$a^{-2}D_\varepsilon^2 = a_2^{(\varepsilon)}, \quad R_{phys} < 0.75 \text{ fm} \tag{11}$$

and

$$a^{-2}D_\varepsilon^2 = \frac{1}{a_2^{(\varepsilon)}}, \quad R_{phys} > 0.75 \text{ fm}. \tag{12}$$

The fit results from the lattices of size $32 \times 12^2 \times 6$ and $40 \times 16^2 \times 8$ together with their derived $a^{-2}D_\varepsilon^2$ have been displayed in Table 2 and Table 3 respectively.

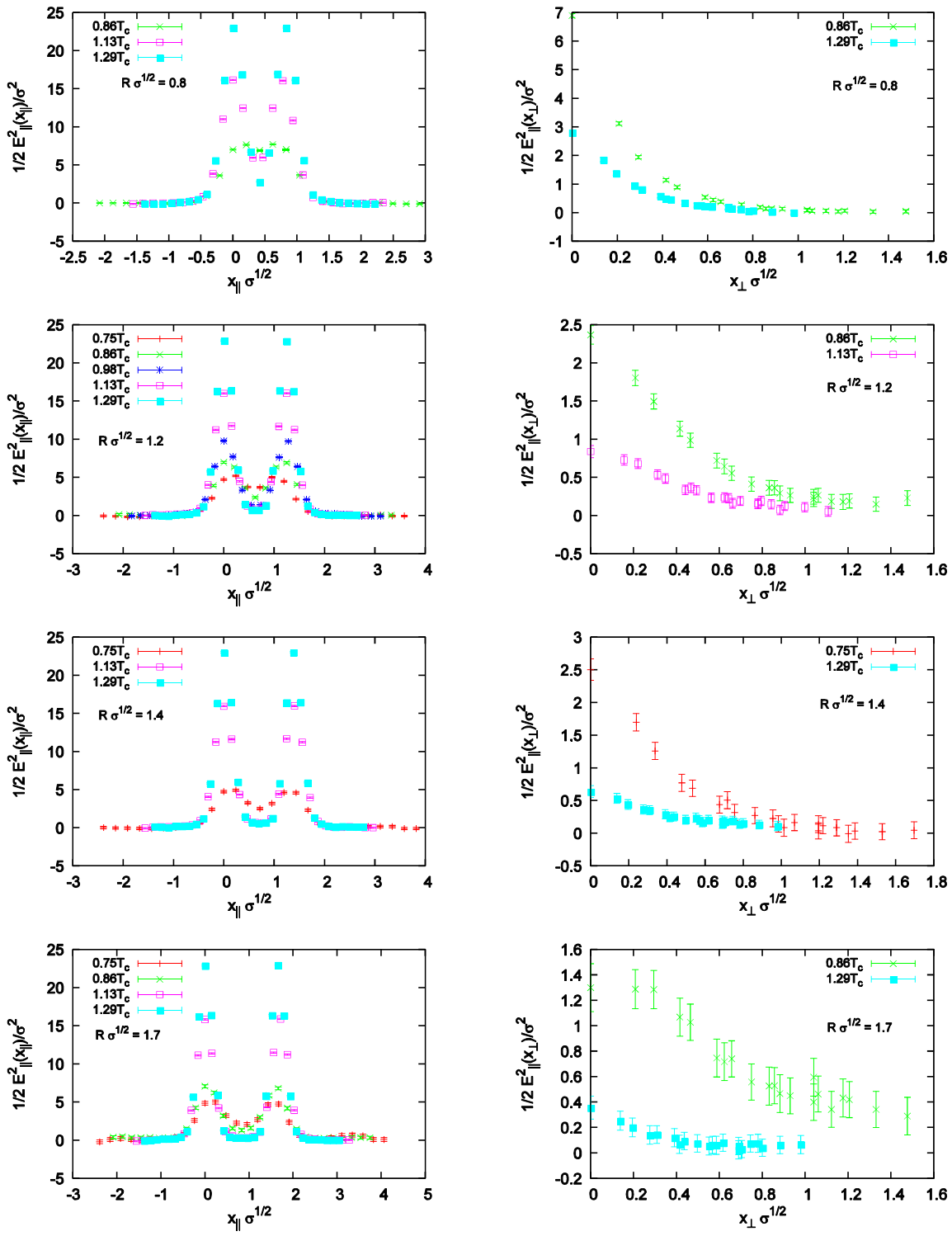

Figure 4. Left: Longitudinal profiles $1/2E_{||}^2(x_{||}, x_\perp = 0)$ *. Right: their transverse profiles* $1/2E_{||}^2(x_{||} = \frac{R}{2}, x_\perp)$ *at* $R\sqrt{\sigma} =$ $0.8, 1.2, 1.4$ *and* 1.7 *from the lattice of size* $40 \times 16^2 \times 8$.

Because of the parameterization dependence of the width for the two parameterizations, the widths calculated by Equation 11 and Equation 12 have to be multiplied by $2\sqrt{2^{1/3} - 1} \approx 1.02$ for coulombic and by $2\sqrt{\ln 2} \approx 1.67$ for Gaussian distribution to connect between the two regimes [8].

Table 2. Results for the fit parameters and $a^{-2}D_\varepsilon^2$ from the lattice of size $32 \times 12^2 \times 6$.

R/a	β	Fit function	a_1	a_2	$a_1^{(\varepsilon)}$	$a_2^{(\varepsilon)}$	$a^{-2}D_\varepsilon^2$	χ^2
4	2.35	Equation 8	7.38(50)	12.56(33)	0.212(18)	2.87(9)	2.87(9)	1.5
	2.39	Equation 8	10.66(89)	16.70(54)	0.105(10)	2.58(8)	2.58(8)	4.3
	2.43	Equation 8	17.29(2.48)	24.49(1.37)	0.068(10)	2.62(13)	2.62(13)	18.5
	2.47	Equation 8	7.71(1.39)	23.42(1.65)	0.040(6)	2.52(12)	2.52(12)	27.2
	2.51	Equation 8	2.41(42)	18.68(1.30)	0.026(3)	2.35(8)	2.35(8)	18.5
6	2.35	Equation 9	31.21(2.34)	21.92(91)	0.00332(21)	0.473(36)	2.11(16)	0.2
	2.39	Equation 8	54.02(7.38)	32.47(1.69)	0.678(191)	7.24(74)	7.24(74)	1.7
	2.43	Equation 8	97.69(17.85)	52.73(3.62)	0.695(189)	9.17(91)	9.17(91)	4.8
	2.47	Equation 8	26.32(4.62)	45.59(3.04)	0.211(47)	7.57(61)	7.57(61)	4.3
	2.51	Equation 8	5.27(1.53)	34.11(3.79)	0.161(38)	7.58(65)	7.58(65)	6.0
8	2.35	Equation 9	43.57(8.07)	27.77(1.95)	0.00173(14)	0.207(28)	4.83(65)	0.1
	2.39	Equation 9	135.17(17.38)	49.06(2.36)	0.00076(5)	0.146(14)	6.85(66)	0.2
	2.43	Equation 9	239.06(43.05)	81.19(5.35)	0.00032(2)	0.103(10)	9.71(94)	0.9
	2.47	Equation 8	89.70(19.41)	83.34(6.60)	1.25(32)	19.13(1.82)	19.13(1.82)	1.1
	2.51	Equation 8	4.71(1.15)	43.03(3.92)	1.18(23)	21.67(1.60)	21.67(1.60)	0.6

Table 3. Results for the fit parameters and $a^{-2}D_\varepsilon^2$ from the lattice of size $40 \times 16^2 \times 8$.

R/a	β	Fit function	a_1	a_2	$a_1^{(\varepsilon)}$	$a_2^{(\varepsilon)}$	$a^{-2}D_\varepsilon^2$	χ^2
4	2.435	Equation 8	3.21(28)	12.03(40)	0.0842(69)	2.49(7)	2.49(7)	0.5
	2.475	Equation 8	2.44(36)	13.59(76)	0.0875(84)	2.77(9)	2.77(9)	1.4
	2.515	Equation 8	5.83(1.03)	21.87(1.51)	0.0491(57)	2.56(10)	2.56(10)	3.2
	2.560	Equation 8	1.63(20)	16.53(77)	0.0204(15)	2.17(5)	2.17(5)	1.6
	2.600	Equation 8	0.82(17)	15.26(1.24)	0.0202(18)	2.27(7)	2.27(7)	3.4
6	2.435	Equation 8	8.83(95)	18.10(75)	0.156(36)	4.39(37)	4.39(37)	0.1
	2.475	Equation 8	9.89(2.06)	23.67(1.87)	2.170(730)	13.41(1.68)	13.41(1.68)	0.6
	2.515	Equation 8	12.54(1.16)	33.88(1.20)	0.301(44)	8.37(45)	8.37(45)	0.2
	2.560	Equation 8	9.27(75)	38.63(1.22)	0.059(7)	5.52(22)	5.52(22)	0.2
	2.600	Equation 8	0.41(18)	17.54(2.96)	0.268(63)	9.86(86)	9.86(86)	1.2
8	2.435	Equation 9	0.572(464)	7.97(2.40)	0.00087(24)	0.200(93)	4.33(71)	0.4
	2.475	Equation 8	42.08(12.54)	44.93(5.07)	156.14(70.66)	67.95(11.51)	67.95(11.51)	0.2
	2.515	Equation 8	78.68(12.32)	73.18(4.34)	0.39(13)	12.31(1.52)	12.31(1.52)	0.2
	2.560	Equation 8	20.69(3.48)	62.84(4.02)	0.23(7)	12.86(1.35)	12.86(1.35)	0.2
	2.600	Equation 8	0.052(29)	11.33(2.36)	6.27(1.37)	40.13(3.35)	40.13(3.35)	0.3

The resulting widths D_ε^2 from the lattices with $N_\tau = 6$ and $N_\tau = 8$ are plotted in Figure 5 as a function of temperature at several values of lattice $q\bar{q}$ separations. As the fit did not work well for R larger than 8a giving too noisy results we did not include them in Figure 5. The width value is given in units of the string tension. Figure 5 shows that at a given value of separation, the width of the flux tube is increasing with the temperature up to around T_c and above T_c it starts to fall again.

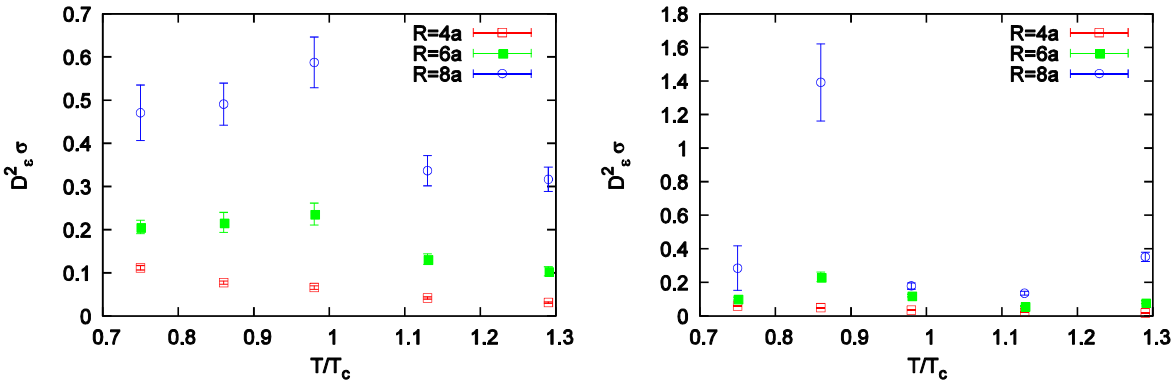

Figure 5. The width of the flux tube as a function of temperature from the lattices of size $32 \times 12^2 \times 6$ and $40 \times 16^2 \times 8$.

If one looks at the R-dependence of the width at temperature, which is plotted in Figure 6, the width broadens when R becomes large. This is in agreement with what is expected from the effective string model prediction about the width as a function of interquark distance R [12]. Figure 6 also confirms the prediction in [15, 16] which stated that the slope of the curve of the linear growth of the width is an increasing function of the temperature.

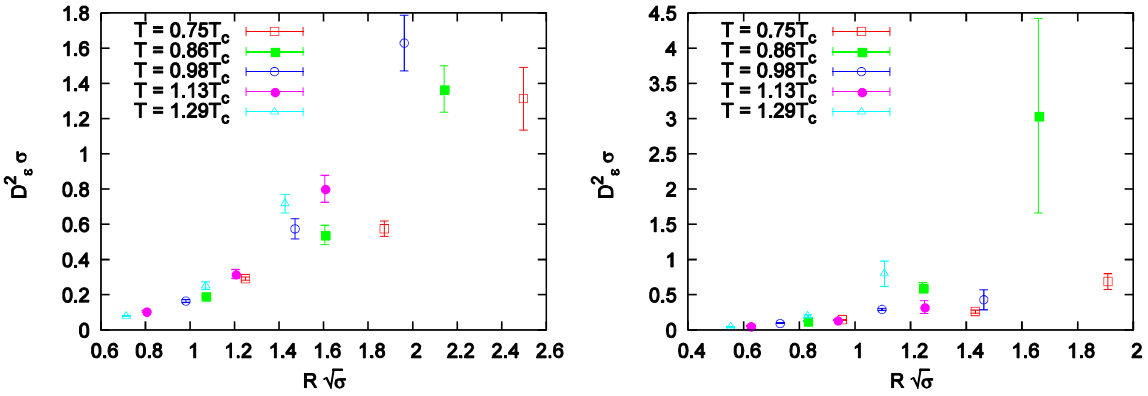

Figure 6. The width of the flux tube as a function of separation from the lattices of size $32 \times 12^2 \times 6$ *and* $40 \times 16^2 \times 8$.

D. Temperature dependent string tension

The decrease of the field strength value on the middle point between the two sources with temperature that was shown by Figure 2 and Figure 4 and also the decrease of the width value with temperature above T_c shown by Figure 5 indicate the gradual disappearance of the flux tube T_c with T. We thus inspect here the temperature dependence of the heavy quark potential. For this purpose, the color averaged potential data between the two sources that has been computed from

$$\langle L(\vec{0})L^{+}(\vec{R})\rangle = e^{-V(|\vec{R}|,T)/T} \qquad (13)$$

is fitted to three types of potentials which are [36]

$$V_1(R,T) = V_0 - \left[\frac{\pi}{12} - \frac{1}{6}\arctan(2RT)\right]\frac{1}{R} + \left[\sigma - \frac{\pi}{3}T^2 + \frac{2}{3}T^2\arctan\left(\frac{1}{2RT}\right)\right] + \frac{T}{2}\ln[1+(2RT)^2] \qquad (14)$$

with a temperature independent string tension. Alternatively, by using two slightly different ansätze both allowing for a temperature dependent string tension $\sigma(T)$,

$$V_2(R,T) = V_0 + \sigma(T)R + \gamma T\ln(2RT) \qquad (15)$$

and

$$V_3(R,T) = V_0 - \frac{\alpha}{R} + \sigma(T)R \qquad (16)$$

with three free parameters. The later one of these includes a $1/R$ piece which accounts for a Coulomb type behaviour for small distances. V_2 features instead a logarithmic behaviour. Both of them include the linear rising part in the potential. These two fits both work well as the data show either a Coulomb or a logarithmic behaviour as well as the linearly rising feature. The results for the free parameters are listed in Table 4, Table 5 and Table 6 respectively.

The potential fits have been done on the lattices with $N_\tau = 6$ and $N_\tau = 8$. The results for $N_\tau = 6$ were previously presented at [37], but the values of the string tension and the other fit parameters have changed slightly because we have included here the data for small separations $R/a = 4$, 5 and 6 at each β and added a whole new data set for $\beta = 2.51$. Thus now for all fits the minimum distance is $R = 4a$ in lattice units. This data addition does affect to the overall fitting procedure that gave the current results.

The resulting string tension values in Table 6 normalized to their zero temperature values are shown in Figure 7, where the leading behavior $\sigma(0) - \pi T^2/3$ in the linear rising part of Equation 14 has been plotted for comparison. The data titled 'previous' is our previous result that was obtained from a lattice of size $24 \times 12^2 \times 6$. From all three data in Figure 7 we see clearly a decreasing string tension with rising temperature.

Table 4. Results for the string tension in the flux tube from fit of the potential to Equation 14.

N_τ	β	T/T_c	aV_0	$a^2\sigma$	χ^2
6	2.35	0.75	0.857(6)	0.103(1)	58.85
	2.39	0.86	0.891(9)	0.063(1)	699.44
	2.43	0.98	0.854(4)	0.0359(4)	504.69
	2.47	1.13	0.758(1)	0.0275(1)	340.13
	2.51	1.29	0.694(3)	0.0260(3)	3386.95
8	2.435	0.75	0.985(5)	0.089(1)	36.33
	2.475	0.86	1.006(7)	0.059(1)	220.21
	2.515	0.98	0.981(3)	0.0368(5)	117.66
	2.560	1.13	0.9018(9)	0.0276(1)	22.57
	2.600	1.29	0.847(2)	0.0258(3)	359.13

Table 5. Results for the string tension in the flux tube from fit of the potential to Equation 15.

N_τ	β	T/T_c	aV_0	$a^2\sigma(T)$	γ	χ^2
6	2.35	0.75	0.857(6)	0.039(2)	1.43(9)	5.83
	2.39	0.86	0.866(4)	0.005(2)	1.45(8)	51.27
	2.43	0.98	0.7936(8)	-0.0053(4)	0.80(2)	16.42
	2.47	1.13	0.6883(2)	-0.0027(1)	0.267(7)	8.28
	2.51	1.29	0.6251(3)	-0.0014(1)	0.117(7)	25.20
8	2.435	0.75	0.967(2)	0.0337(8)	1.23(3)	0.47
	2.475	0.86	0.9786(3)	0.0043(1)	1.296(5)	0.07
	2.515	0.98	0.9270(7)	-0.0060(4)	0.829(17)	2.17
	2.560	1.13	0.8331(7)	-0.0046(4)	0.373(19)	8.68
	2.600	1.29	0.7755(6)	-0.0033(3)	0.225(15)	13.88

Table 6. Results for the string tension in the flux tube from fit of the potential to Equation 16.

N_τ	β	T/T_c	aV_0	$a^2\sigma(T)$	α	χ^2
6	2.35	0.75	1.023(23)	0.059(2)	0.69(6)	10.91
	2.39	0.86	1.063(23)	0.022(1)	0.78(7)	117.68
	2.43	0.98	0.916(8)	0.0031(5)	0.47(3)	82.92
	2.47	1.13	0.7312(7)	-0.00011(4)	0.165(3)	2.98
	2.51	1.29	0.6446(5)	-0.00034(3)	0.075(2)	4.51
8	2.435	0.75	1.113(4)	0.0498(3)	0.61(1)	0.29
	2.475	0.86	1.147(9)	0.0201(6)	0.68(2)	6.53
	2.515	0.98	1.042(2)	0.0035(1)	0.457(7)	1.48
	2.560	1.13	0.8871(8)	-0.00049(5)	0.212(2)	0.56
	2.600	1.29	0.8087(12)	-0.00084(8)	0.130(4)	2.76

The deviation between $\sigma(T)/\sigma(0)$ data and the leading behavior $\sigma(0) - \pi T^2/3$ reflects the thermal corrections of the temperature-dependent terms to the zero temperature string tension. When precision is improved, i.e. the lattice spacing is decreased $\sim 1/N_\tau$ the string tension value becomes smaller compared to its previous value.

IV. CONCLUSION

We have investigated longitudinal and transverse profiles of the chromoelectric and chromomagnetic components of the field strength in the flux tube at temperatures around the deconfinement phase transition using Polyakov loop-plaquette correlations in the lattice gauge theory.

Monte Carlo numerical simulations have been performed in SU(2) pure gauge theory at temperatures $0.75T_c - 1.29T_c$ separating a quark and an antiquark by distances $0.2\text{fm} - 2.3\text{fm}$. We were able to follow a clear signal for the flux tube over almost twice a larger distance than in our previous work. This was due to our implementation of a CUDA programming code for our flux tube simulation on a GPU accelerator. As a result we reached much higher statistics at the same time. This higher statistics allowed us to redetermine the numerical values of the following observables with higher accuracy.

Results on longitudinal profiles from two different lattices show that the field strength value at the middle point between the two sources or the height of the flux tube clearly decreases with rising temperature. The distribution approaches the one of two isolated quarks as the temperature goes to T_c. This is in agreement with what we expect that the

flux tube is expected to exist only in the confined phase.

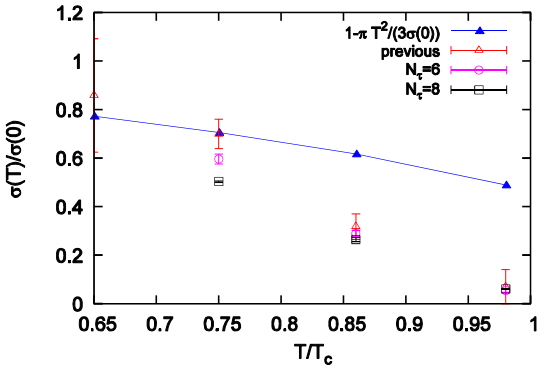

Figure 7. The string tension as obtained from fits with Equation 16, normalized to its zero temperature value.

By doing fits to the transverse profiles we have determined the physical width of the flux tube as a function of temperature. The physical width of the flux tube measured from lattices of two different lattice spacings both increases with temperature until T_c, which looks rather different from previous work that showed a gradual decrease instead. The current results with higher accuracy confirm the prediction in [15, 16] which stated that the slope of the curve of the linear growth of the width with separation is an increasing function of the temperature. Thus one has to conclude that the height and width of the flux tube do not decrease at the same time with temperature below T_c but they do above T_c.

We also tried to determine temperature dependent string tension values from the potential between the two sources by doing three types of fit to the potential data obtained at two different lattice spacings. All the string tension results clearly decrease with rising temperature. Our string tension results have been compared with the previous results that were obtained from the lattice of size $24 \times 12^2 \times 6$ as well as with the lowest-order temperature effect on the linear part of the potential. As the lattice becomes larger and finer, at the improved precision, the temperature dependent string tension tends to attain smaller values than on the smaller and coarser lattice.

ACKNOWLEDGMENTS

This study is carried out as becoming an objective of the project "The Lattice Numerical Simulations of the Strong Interaction" (SSA 019/14) which initialized the lattice field theory research in Mongolia. This was made possible for the first time in 2014 as the project approved by the Ministry of Education, Culture, Science and Sports of Mongolia. We also would like to acknowledge the Mongolian Foundation for Science and Technology for their financial support during the time of the project.

REFERENCES

[1] H. D. Politzer, Phys. Rev. Lett. **30**, 1346 (1973).

[2] D. J. Gross and F. Wilczek, Phys. Rev. Lett. **30**, 1343 (1973).

[3] L. D. McLerran and B. Svetitsky, Phys. Lett. B **98** 195 (1981).

[4] J. Kuti, J. Polonyi and K. Szlachanyi, Phys. Lett. B **98**, 199 (1981).

[5] Y. Aoki *et al*., J. High Energy Phys. **06**, 088 (2009).

[6] A. Bazavov *et al*., Phys. Rev. D **85**, 054503 (2012).

[7] R. W. Haymaker and J. Wosiek, Phys. Rev. D **43**, 2676 (1991).

[8] G. S. Bali, K. Schilling K and Ch. Schlichter, Phys. Rev. D **51**, 5165 (1995).

[9] R. W. Haymaker, V. Singh and Y. Peng, Phys. Rev. D **53**, 389 (1996).

[10] A. M. Green, C. Micheal and P. S. Spencer, Phys. Rev. D **55**, 1216 (1997).

[11] M. Luscher, K. Symanzik and P. Weisz, Nucl. Phys. B **173**, 365 (1980)

[12] M. Luscher, G. Munster and P. Weisz, Nucl. Phys. B **180** [FS2], 1 (1980).

[13] H. B. Nielsen and P. Olesen, Nucl. Phys. B **61**, 45 (1973).

[14] M. Gaselle, F. Gliozzi, U. Magnea and S. Vinti, Nucl. Phys. B **460**, 397 (1996).

[15] A. Allais, M. Gaselle, J. High Energy Phys. **01**, 073 (2009).

[16] M. Gaselle, J. High Energy Phys. **08**, 063 (2010).

[17] M. Gasselle and P. Grinza, J. High Energy Phys. **11**, 174 (2012).

[18] S. Chagdaa, Ph.D. thesis, Bielefeld University, 2008. (https://pub.uni-bielefeld.de/publication/2303220)

[19] P. Cea, L. Cosmai, F. Cuteri and A. Papa, J. High Energy Phys. **06**, 033 (2016).

[20] P. Bicudo, N. Cardoso and M. Cardoso (arXiv:hep-lat/1702.03454).

[21] M. Luscher and P. Weisz, J. High Energy Phys. **09**, 010 (2001).

[22] M. Fukugita and T. Niuya, Phys. Lett. **132B**, 374 (1983).

[23] S. Chagdaa, Pos(LATTICE 2007) **172**, 4 (2007).

[24] L. H. Ryder, Quantum Field Theory 2nd (Cambridge University Press, 1996).

[25] M. Creutz, Phys. Rev D **21**, 2308 (1980).

[26] M. Creutz, Phys. Rev. Lett. **43**, 553 (1979).

[27] A. D. Kennedy and B. J. Pendleton, Phys. Lett. B **156**, 393 (1985).

[28] M. Creutz, Phys. Rev. D **36**, 515 (1987).

[29] P. de Forcrand and O. Jahn, (arXiv:hep-lat/0502041) (2005).

[30] G. Parisi, R. Petronzio and F. Rapuano, Phys. Lett. B **128**, 418 (1983).

[31] R. W. Haymaker and Y. Peng, Phys. Rev. D **47**, 5104 (1993).

[32] N. Cardoso and P. Bicudo, J. Comput. Phys. **230**, 3998 (2011).

[33] S. Chagdaa, E. Laermann, G. Gombojav and E. Galsandorj, Mongolian Journal of Physics **1**, 33 (2016).

[34] J. Engels, J. Finberg and D. Miller, Nucl. Phys. B **387**, 501 (1992).

[35] R. Sommer, Nucl. Phys. B **291**, 673 (1988).

[36] M. Gao, Phys. Rev. D **40**, 2708 (1989).

[37] S. Chagdaa, E. Laermann, G. Gombojav, E. Galsandorj and B. Purevragchaa, The 13th international eXtreme QCD conf. (China: Wuhan, 2015). (http://conf.ccnu.edu.cn/~xqcd2015/posters/Chagdaa_XQCD2015.pdf).